UvA-DARE (Digital Academic Repository)

Surface Decomposition of Doped PrBaMn2O5+δInduced by in Situ Nanoparticle Exsolution

Quantitative Characterization and Catalytic Effect in Methane Dry Reforming Reaction

Cao, Xiaojuan; Ke, L.; Zhao, K.; Yan, X.; Wu, X.; Yan, N.

Citation for published version (APA):

Cao, X., Ke, L., Zhao, K., Yan, X., Wu, X., & Yan, N. (2022). Surface Decomposition of Doped PrBaMn$_2$O$_{5+\delta}$Induced by in Situ Nanoparticle Exsolution: Quantitative Characterization and Catalytic Effect in Methane Dry Reforming Reaction. *Chemistry of Materials*, *34*(23), 10484–10494. https://doi.org/10.1021/acs.chemmater.2c02488

Surface Decomposition of Doped PrBaMn$_2$O$_{5+\delta}$ Induced by *In Situ* Nanoparticle Exsolution: Quantitative Characterization and Catalytic Effect in Methane Dry Reforming Reaction

Xiaojuan Cao, Le Ke, Kai Zhao, Xiaoyu Yan, Xiaoyu Wu, and Ning Yan*

Read Online

ACCESS | Metrics & More | Article Recommendations | SI Supporting Information

ABSTRACT: The exsolution of metallic nanoparticles (NPs) from perovskite oxides is a promising strategy for synthesizing supported catalysts. The associated segregation of A-site cations on the surface is challenging to investigate experimentally and is often detrimental to the catalytic performance. In this work, we found that during the *in situ* exsolution of Ni-Co bimetallic nanoparticles from Pr$_{0.45}$Ba$_{0.45}$Mn$_{1-x}$(Co$_{1/3}$Ni$_{2/3}$)$_x$O$_{3\pm\delta}$, A-site cation enrichment occurred on the surface when x is 0.1; yet, the perovskite surface decomposed when x reached 0.2, forming a thin layer comprising various nanocrystalline oxides, which partially blocked the active sites of the exsolved Ni-Co particles. A hydration and carbonation reaction facilitated the conversion of nanocrystalline BaO species into large and highly crystallized BaCO$_3$ particles. This enabled the exposure of more Ni-Co active sites and offered a chance to quantify that the decomposed surface layer accounts for ∼7.2 wt % of the total perovskite. Because of this unique feature, the surface-decomposed catalyst showed higher activity in the dry methane reforming reaction with better stability. Importantly, the regeneration feature was not hampered as the complete exsolution-dissolution recyclability of the catalyst remained.
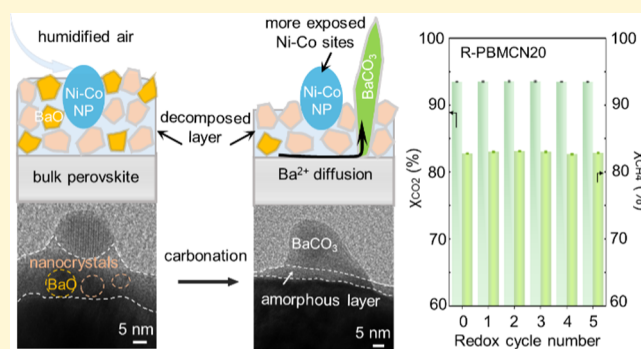
1. INTRODUCTION

Supported metal catalysts are extensively used in various chemical and energy-conversion processes.[1−3] The solid support not only offers a high surface area to enable the robust mono-dispersion of metallic nanoparticles (NPs), but importantly, also creates the metal-support interaction, manipulating the selectivity and activity of the catalysts. In the industrial operation, all catalysts inevitably suffer from activity degradation due to various mechanisms such as poisoning, fouling, coking, and NP sintering.[4−6] Unfortunately, the regeneration of the spent catalysts remains a grand challenge: some of the degradations are fully irreversible; many regeneration processes also lead to the structural degradation of the catalyst. In the real-life practice, it is common that such spent catalysts are subjected to the "recycling" process to retrieve the precious metals and minerals. An efficient regeneration to restore the performance of the deactivated catalysts thus features high on the wish list of both academia and industry.

In this context, a new strategy of preparing the supported metal catalysts, namely, metallic NP exsolution,[7−9] came under the spotlight. Upon changes in the atmosphere at elevated temperatures, specific dopants can precipitate out from the host matrix. The readily formed metallic NPs become the active species for catalytic reactions. This approach was first proposed in 2002 using a perovskite oxide as the host,[10] which enabled the *in situ* self-regeneration (upon the redox cycle) and long lifetime of the catalysts ("socketed" NPs by the matrix). Today, by tuning the non-stoichiometry, selecting proper B-site dopants, and pretreating the host perovskite, various monometallic and multi-metallic NPs can be successfully exsolved from the perovskite oxide matrix, showing unique catalytic performance in many industrially relevant reactions, including methane reforming,[11−13] water splitting,[14,15] and water−gas-shift reactions.[16] However, due to reasons such as the generation of additional oxygen vacancies and the change of stoichiometry, the exsolution of B-site cations at high temperature easily induces the segregation of A-site cations on the surface.[17,18] Although this segregated layer is often thin, it has been widely documented to have a drastic influence on the (electro)activity of the catalyst. For instance, the 10-nm Sr-enriched layer in a SrTi$_{1-x}$Fe$_x$O$_{3-\delta}$ thin film reduced the rate of oxygen exchange reaction by several orders of magnitude.[19,20]
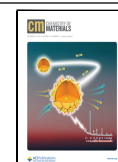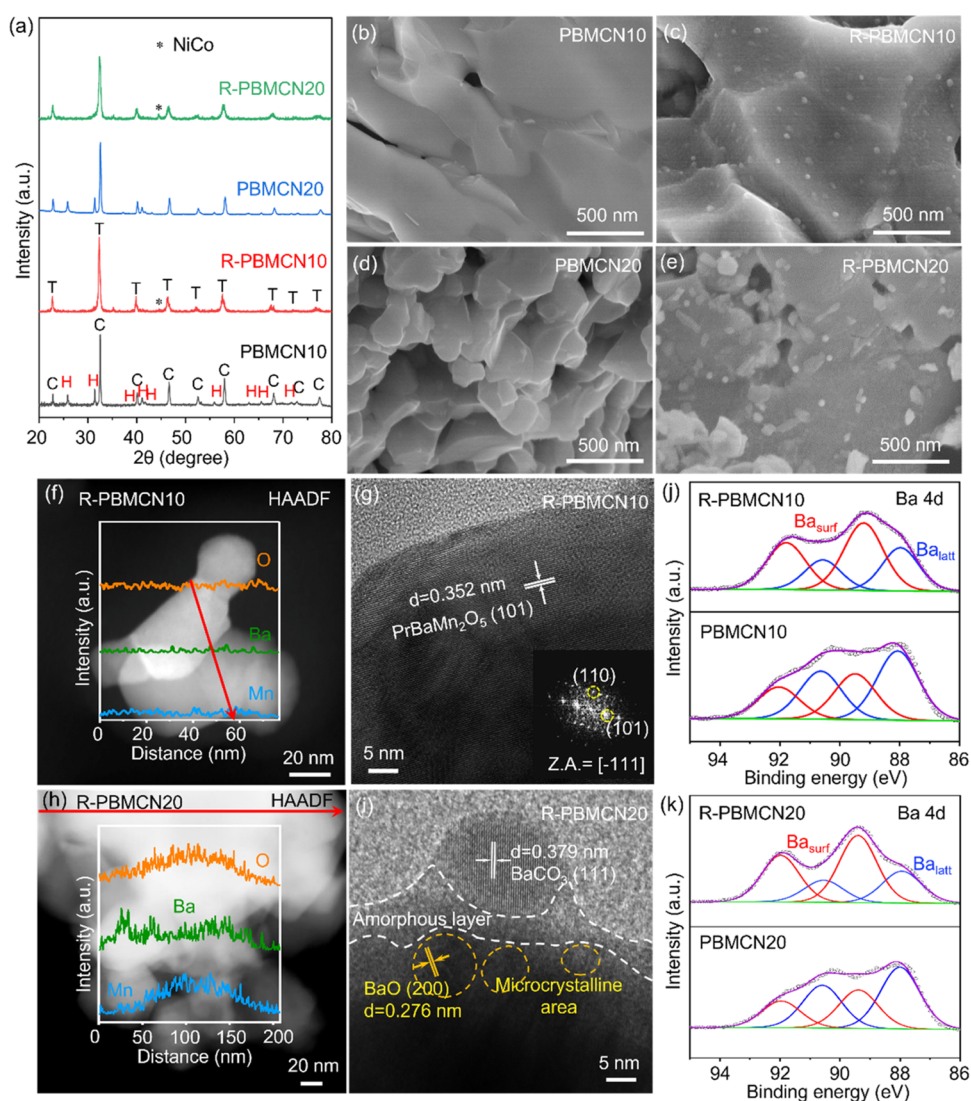
Figure 1. (a) XRD patterns and (b−e) cross-sectional SEM images of PBMCN10, R-PBMCN10, PBMCN20, and R-PBMCN20; (f−i) HAADF and HRTEM images of R-PBMCN10 and R-PBMCN20; the insets in (f) and (h) are the corresponding EDX elemental line scans; the area marked by the white dash lines in (i) is the amorphous domain; XPS spectra comparison of Ba 4d for (j) PBMCN10 and R-PBMCN10, (k) PBMCN20 and R-PBMCN20.

Barium segregation in cation-ordered $LnBaCo_2O_{5+\delta}$ perovskites (Ln = lanthanide) became kinetically faster at temperatures >400 °C, leading to the decrease of transition metal surface coverage.[21] We also report the surface amorphization and decomposition of $PrBa_{0.85}Ca_{0.15}MnFeO_{5+\delta}$ during the electrochemical water splitting reaction.[22] Nonetheless, as cation segregation and surface decomposition typically occur on the surface layers that are a few nanometers thick, it remains challenging to (quantitatively) investigate this thin layer in detail.

In this work, we found that the *in situ* exsolution of Ni-Co bimetallic nanoparticles from $Pr_{0.45}Ba_{0.45}Mn_{1-x}(Co_{1/3}Ni_{2/3})_xO_{3\pm\delta}$ induced different surface changes. A-site cation enrichment on the surface occurred when x was 0.1; yet, the perovskite surface decomposed when x reached 0.2. The mass ratio of the decomposed perovskite was determined quantitatively. In the dry methane reforming reaction, the origin of the higher activity and the regeneration capability of the surface-decomposed catalysts were explored.

2. RESULTS AND DISCUSSION

2.1. Surface Evolution Induced by Exsolution. In this study, we selected $PrBaMn_2O_{5+\delta}$ (PBM) as the model system to study the process of exsolution. This host oxide demonstrates good stability in the reducing atmosphere, yet enjoys abundant oxygen vacancies (linear clusters). Co and Ni (Co/Ni = 0.5) were used as the B-site doping elements for the exsolution. This bimetallic catalytic system has been well examined in the literature and our previous work,[23,24] which outperformed Ni in the methane dry reforming reaction (DRM) in terms of activity and coking resistance. As the exsolution of the B-site transition metal nanoparticles can be facilitated by the A-site deficiency, we used the A-site-deficient $Pr_{0.45}Ba_{0.45}Mn_{1-x}(Co_{1/3}Ni_{2/3})_xO_{3\pm\delta}$, which contained 10% of A-site vacancy. Note that such A-site deficiency is also beneficial in suppressing the A-site cation surface segregation.[25,26] Figure 1a shows the X-ray diffraction (XRD) patterns of the as-prepared (PBMCN10, x = 0.1; PBMCN20, x = 0.2) and reduced perovskite oxides (R-PBMCN10 and R-PBMCN20), respectively. The characteristic peaks in the

PBMCN10 and PBMCN20 patterns suggested the mixed cubic and hexagonal perovskite phases. After the reduction in 5% H_2/Ar at 800 °C for 4 h, the peaks belonging to the hexagonal phase disappeared completely, and the diffraction peaks of the cubic phase shifted slightly to the left, indicating the lattice expansion due to the phase transformation to the double-perovskite structure.[27,28] This double-perovskite phase transformation can be shown by the reaction below, where "C" represents the cubic phase and "H" represents the hexagonal phase

$$Pr_{0.5}Ba_{0.5-0.5x}Mn_{1-0.5x}O_{3+\delta}(C) + 0.5xBaMnO_3(H)$$
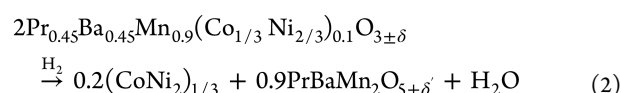$$\xrightarrow{H_2} 0.5PrBaMn_2O_{5+\delta} \tag{1}$$
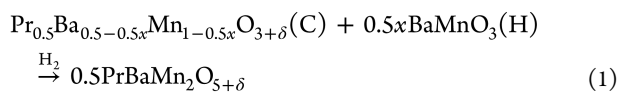
In addition, the diffraction peak at 44.5° (see the enlarged patterns in Figure S1), indexed to the (111) plane of Ni-Co alloy,[29] revealed that the bulk bimetallic phase formed after the reduction. No other impurities have been detected in either R-PBMCN10 or R-PBMCN20 from the XRD patterns.

We then used the microscopic technique to monitor the microstructural change during the exsolution processes. In the scanning electron microscopy (SEM) images shown in Figures 1b−e, the as-prepared PBMCN10 and PBMCN20 show clean fractural surfaces. The reduction at 800 °C indeed caused the exsolution of small NPs in both samples, sizing between 20 and 50 nm. Transmission electron microscopy (TEM) was also applied to further reveal the microstructure and composition change. Indeed, the exsolved Ni-Co bimetallic nanoparticles were clearly visible in both R-PBMCN10 and R-PBMCN20 (see the high-resolution TEM micrographs in Figure S2). The distribution of all of the constituent elements in R-PBMCN10 was rather uniform, as reflected by the energy-dispersive X-ray spectroscopy (EDX) analysis in Figure 1f. The HRTEM micrograph in Figure 1g shows that the surface of R-PBMCN10 remained intact after reduction; the interplanar spacing was 0.352 nm, which corresponded to the (101) plane of PBM. The fast Fourier-transformed image (FFT) in the inset confirmed the $[\bar{1}11]$ zone axis of the examined crystal.
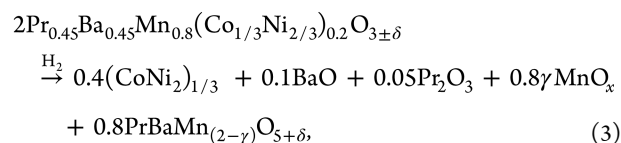
On the contrary, R-PBMCN20 showed a nonuniform elemental distribution (see the elemental mappings in Figure S3), particularly for Ba and O along the direction of the line in Figure 1h (see the corresponding EDX elemental line scan in the inset). In the HRTEM micrograph in Figure 1i, a thin amorphous layer on the surface was identified. Such a feature was also prominent in other examined particles, as shown in Figure S4. In addition to this amorphous layer, we also observed other microcrystals with size below 10 nm near the surface. For instance, the circled microcrystalline domains in Figure 1i show a d-spacing of 2.76 Å, matching the (200) plane of BaO. Additional domains with clear interplanar spacings are summarized in Figure S4, implying the presence of other oxides, including MnO, Mn_2O_3, and Pr_2O_3. It should be noted that a protruded nanoparticle from the surface was not the exsolved nanoparticle: the interplanar spacing was 3.79 Å, which can be indexed to the (111) plane of $BaCO_3$. Its formation was due to the reaction between BaO and atmospheric CO_2 (see more discussions below). All of these surface characteristics indicated that the Ni-Co nanoparticle exsolution from PBMCN20 has induced the surface decomposition.

We also used X-ray photoelectron spectroscopy (XPS) to probe the surface composition and chemical states. In the deconvoluted Ba 4d spectrum in Figure 1j,k, we noticed the

migration of Ba cations from the bulk lattice (BE = 88.07 eV for Ba $4d_{5/2}$ of Ba_{latt}) to the surface (BE = 89.51 eV for Ba $4d_{5/2}$ of Ba_{surf}) after the nanoparticle exsolution for both samples. The atomic ratios of Ba_{suf}/Ba_{latt} increased from 0.7 to 1.7 for PBMCN10 and from 0.6 to 2.1 for PBMCN20 after the reduction (see the summary in Figure S5 and Table S1). Note that the signal-to-noise ratio of Ni 2p spectra was rather low due to the low doping ratio. Yet, the signal intensities of Ni 2p in the reduced samples were apparently lower compared with those before reduction, $e.g.$, the ratio of Ni decreased significantly ($ca.$ 40%) in R-PBMCN20 compared with that in PBMCN20. This might be attributable to the fact that the products of the surface decomposition have partially blocked the exsolved Ni-Co nanoparticles. Based on the microscopic and surface spectroscopic results above, we concluded that the nanoparticle exsolution from PBMCN10 has induced the surface enrichment of Ba (see eq 2).

$$2Pr_{0.45}Ba_{0.45}Mn_{0.9}(Co_{1/3}Ni_{2/3})_{0.1}O_{3\pm\delta}$$
$$\xrightarrow{H_2} 0.2(CoNi_2)_{1/3} + 0.9PrBaMn_2O_{5+\delta'} + H_2O \tag{2}$$

Yet, the surface decomposition occurred in R-PBMCN20; a possible reaction is shown below

$$2Pr_{0.45}Ba_{0.45}Mn_{0.8}(Co_{1/3}Ni_{2/3})_{0.2}O_{3\pm\delta}$$
$$\xrightarrow{H_2} 0.4(CoNi_2)_{1/3} + 0.1BaO + 0.05Pr_2O_3 + 0.8\gamma MnO_x$$
$$+ 0.8PrBaMn_{(2-\gamma)}O_{5+\delta}, \tag{3}$$

Compared with eq 2 with only 10 atom % B-site cations exsolution and the subsequent formation of stoichiometric perovskite, the exsolution of 20 atom % B-site cations in R-PBMCN20 induced A-site cation excess, which made the perovskite thermodynamically less stable. Hence, the surface decomposition occurred. Nonetheless, the bulk PBM perovskite remained stable in both samples after the reduction.

As the exsolution-induced surface decomposition generated a thin layer containing various nanocrystalline oxides, it is yet challenging to characterize this layer quantitatively. To enable this investigation, we were inspired by the formation of interfacial $BaCO_3$ species (see Figure 1i) and designed an aging process in humidified air at the ambient condition to convert small BaO nanocrystals into highly crystalized $BaCO_3$ (aging at higher temperature or with higher CO_2 concentration might induce additional surface decomposition). Assuming the complete carbonation of BaO species in the decomposed layer, we can quantify the resulting carbonate to study the amount of the decomposed perovskite. Indeed, the carbonation will occur exclusively for BaO: the equilibrium constants (K) of all the possible carbonation reactions in the decomposition layer were compared in Figure 2a, from which we can deduce that the BaO carbonation reaction is extremely faster and more complete than all of the other reactions. The presence of water vapor has been confirmed to "catalyze" the carbonation reaction in our and others' previous work. From the chemical point of view, adsorbed water acts as a reactant and solvent to accelerate the formation of the transient hydroxyl compound, which is more reactive for the chemisorption of CO_2 than metal oxides.[30,31] From the mechanical point of view, water vapor could facilitate the formation of a loose and porous structure, enabling the faster diffusion of ion/gas and enhancing the carbonation.[32−34] Accompanied by the surface migration of Ba species, the carbonation reaction resulted in
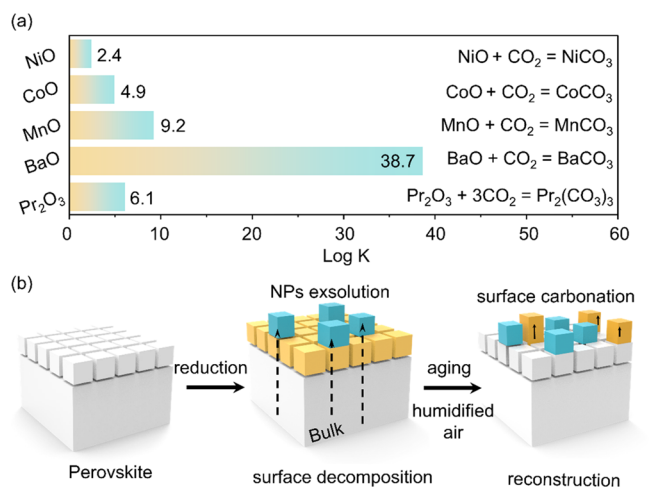
Figure 2. (a) Equilibrium constants comparison of possible carbonation reactions in the decomposition layer; (b) schematic of the surface evolution of the PBMCN20 perovskite oxide catalyst *via in situ* exsolution and aging process for quantitative analysis.

the formation of large and highly crystallized $BaCO_3$ particles *viaeq 4*, facilitating the quantitative study (*vide infra*).

$$BaO + CO_2 \xrightarrow{H_2O} BaCO_3 \text{ (surface reaction)} \quad (4)$$
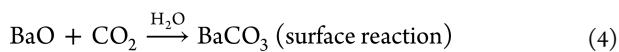
The schematic surface evolution process of PBMCN20 perovskite oxide *viain situ* exsolution and aging can be illustrated in Figure 2b.

Figure 3a shows the XRD patterns of the aged perovskite oxides (AR-PBMCN10 and AR-PBMCN20). After aging in humidified air (RH = 98%) at ambient conditions, $BaCO_3$ appeared in AR-PBMCN20, whereas no change occurred in AR-PBMCN10. The corresponding microscopic images unveiled that compared with AR-PBMCN10 (Figure 3b), the surface of AR-PBMCN20 showed plenty of newly formed nanorods, which were deduced as $BaCO_3$ (see the black arrows in Figure 3c). To confirm their chemical composition, we analyzed the sample using the TEM. The high-angle annular dark field (HAADF) image and EDX elemental mappings in Figure 3d again confirmed the presence of exsolved Ni-Co NPs (marked with white circles). The rod-like structures (marked with dotted red frames) in AR-PBMCN20 were relatively large (*cf.* BaO nanocrystals in Figure 1i) in size and only contained Ba, C, and O. The interplanar spacing was 3.78 Å, which can be indexed to the (111) plane of $BaCO_3$ (see the HRTEM micrograph in Figure 3e). BaO species were not observable anymore in the TEM micrographs (also see Figure S4e), implying that this aging process transformed all of the BaO into carbonate.

This conclusion was aligned with the XPS analysis in Figure S6 and Table S2, which also confirmed the presence of
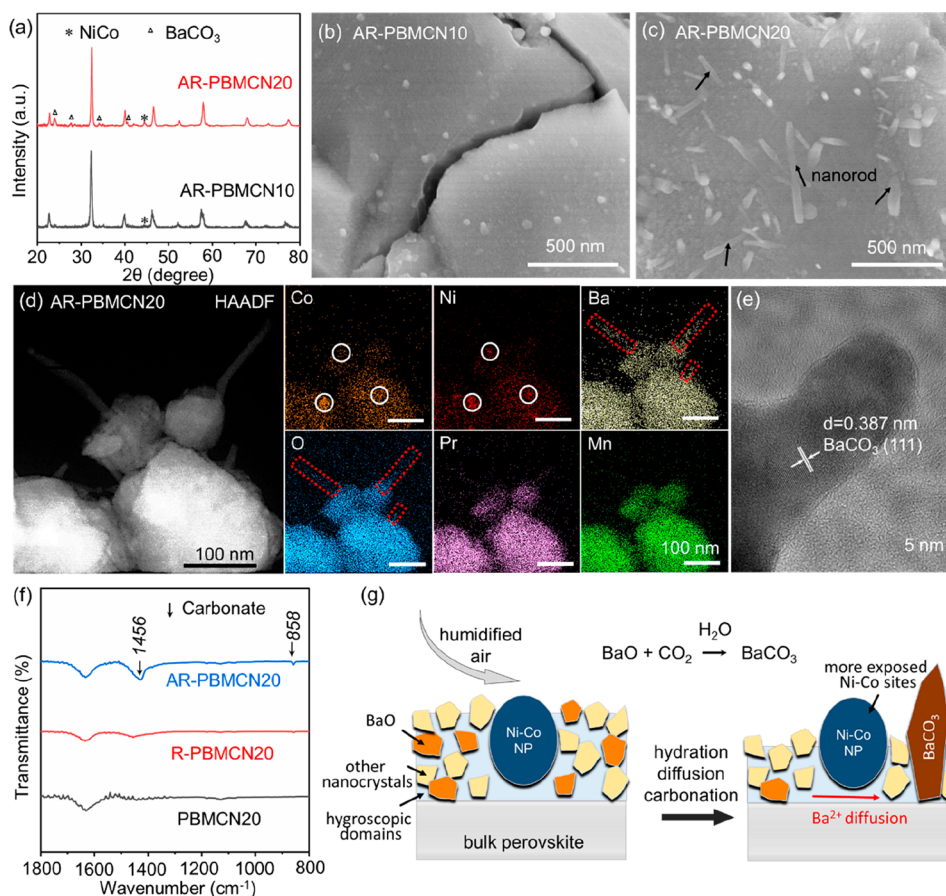
Figure 3. (a) XRD patterns and (b, c) SEM images of AR-PBMCN10 and AR-PBMCN20; (d) HAADF image and the corresponding EDX elemental mappings of Co, Ni, Ba, O, Pr, and Mn, respectively; the circles indicate the area of Co-Ni alloy and the dotted red frames indicate surface carbonate; (e) HRTEM image of the carbonate on the surface of AR-PBMCN20; (f) FTIR spectra of PBMCN20, R-PBMCN20, and AR-PBMCN20; (g) schematic of Ba mitigation and carbonation process in the decomposed layer during aging.

Figure 4. XRD Rietveld refinements of (a) R-PBMCN10, (b) AR-PBMCN10, (c) R-PBMCN20, and (d) AR-PBMCN20; (e) weight fractions of multiple phases obtained from the Rietveld analysis; (f) TGA curve of AR-PBMCN20.

carbonate in AR-PBMCN20. It seems that the formation of large carbonate crystals was beneficial for "unblocking" the Ni and Co sites: the surface ratio of Ni increased to 0.8 atom %, whi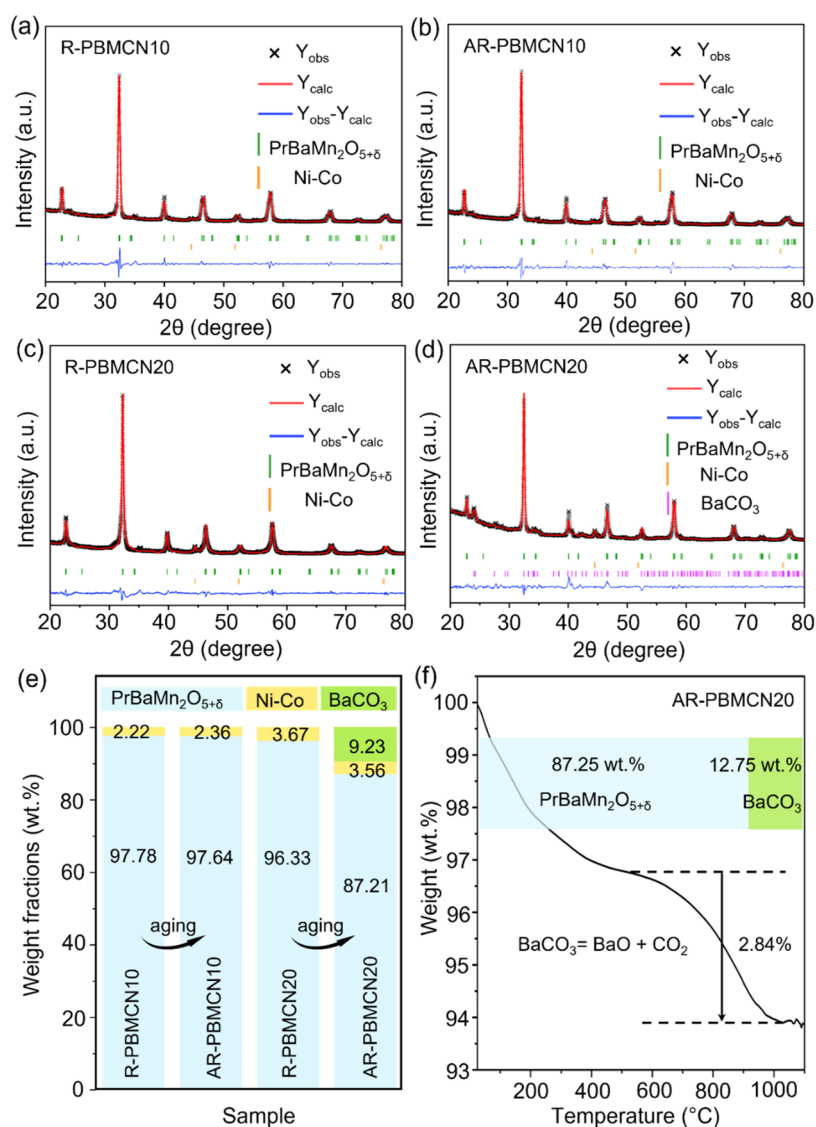ch was comparable with that before the exsolution (0.7 atom %). In addition, we used the Fourier-transformed infrared spectroscopy (FTIR) to further examine the surface. As shown in Figure 3f, the strong peaks at 1456 and 858 cm^{-1} in AR-PBMCN20 corresponded to the asymmetric stretching vibrations of the carbonate groups.[35,36] Other samples including AR-PBMCN10, however, only had the peaks related to the OH functionality (also see Figure S7). Therefore, we concluded that the aging process indeed converted the BaO species in R-PBMCN20 into large carbonate crystals. The hypothetical mechanism is shown in Figure 3g. In humidified air, the hygroscopic nature of BaO enabled the absorption of moisture and the formation of "wet" hydrated domains where the chemisorption of CO_2 was promoted and the faster diffusion of Ba^{2+} was enabled. Therefore, the carbonation reaction may follow the so-called microcrucible mechanism, resulting in the formation of large carbonate nanorods.[37]

Because of the significant aggregation of Ba species, more Ni-Co sites were subsequently exposed (*cf.* XPS results).

2.2. Quantitative Characterization of Exsolution and Surface Decomposition.
In order to quantitatively analyze the decomposed surface layer, we performed Rietveld refinement of the XRD diffraction data together with the thermogravimetric analysis. The refinement results are shown in Figures 4a−e and S8, and summarized in Table S3. In R-PBMCN10, the exsolved Ni-Co NPs accounted for 2.2 wt % which was very close to the maximum theoretical value of 2.6 wt % assuming the complete exsolution of all Ni and Co cations. As a comparison, 3.7 wt % of Ni-Co NPs presented in R-PBMCN20 after reduction, which was also less than the maximum theoretical value (5.1 wt %). In AR-PBMCN20, 9.23 wt % of $BaCO_3$ was identified, which suggested that 8.67 atom % of the PBM host perovskite oxide had decomposed.

To confirm our conclusion, we also used thermogravimetric analysis (TGA) to examine AR-PBMCN20 (Figure 4f). The weight loss before 400 °C was attributable to the removal of (hydrated)water as all nanocrystals in the decomposed layer are highly hygroscopic. The other weight loss starting at ~600
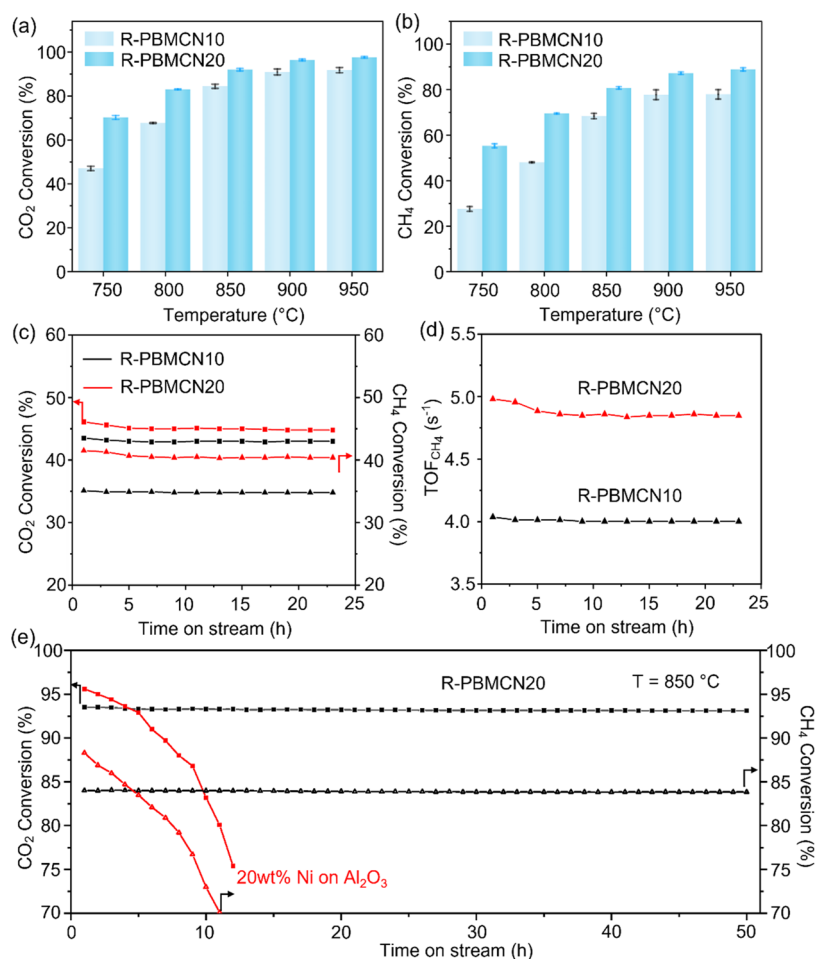
Figure 5. (a) CO_2 and (b) CH_4 conversion of R-PBMCN10 and R-PBMCN20 at various temperatures; (c) CO_2 (square) and CH_4 (triangle) conversions and (d) TOF_{CH_4} of R-PBMCN10 and R-PBMCN20 as a function of time on stream at 850 °C; $CH_4/CO_2/N_2$ = 25:25:50 mL min^{-1}; catalyst loading is 50 mg; (e) comparison of R-PBMCN20 and 20 wt % Ni on Al_2O_3 at 850 °C. Other than where specified, the feedstock is $CH_4/CO_2/N_2$ = 10:10:80 mL min^{-1} and the catalyst loading is 70 mg.

°C was ascribed to the thermal decomposition of $BaCO_3$ nanocrystals and the change of oxygen stoichiometry.[38] The weight loss was 2.8 wt %, corresponding to 12.75 wt % of $BaCO_3$ in AR-PBMCN20. This value was slightly higher than that obtained from the Rietveld analysis as the loss of oxygen also contributed to this weight loss. We plotted the average thickness of the decomposed layer as a function of the perovskite particle diameter (assuming spherical particles; see Figure S9). This layer was from 4 to 15 nm, which agreed with the thickness reported elsewhere.[20,39−42]

2.3. Catalytic Performance and Regeneration. To evaluate the catalytic effect of the surface-decomposed catalyst, we selected methane dry reforming as the model reaction. The conversions of both CO_2 and CH_4 are shown as a function of the reaction temperatures in Figures 5a,b. CO_2 and CH_4 conversions increased as the temperature rose up. The CO_2 conversion was slightly higher than the CH_4 conversion due to the side reactions like reverse water−gas shift reaction (RWGS),[43] which could consume CO_2 at high temperatures. The catalytic selectivity was presented by the hydrogen-to-carbon monoxide (H_2/CO) ratio in the effluent; a high H_2/CO was achieved for both catalysts above 850 °C (see Figure S10). Interestingly, it seems that R-PBMCN20 with partial blockage of Ni-Co sites showed even better catalytic activity than R-PBMCN10: the former exhibited higher conversion of

CO_2 and CH_4 at all of the examined temperatures ranging from 750 to 950 °C compared with that of R-PBMCN10 without the A-site alkaline earth oxides on the surface. The error bars represented the standard errors of the mean conversion, which were obtained from the 30 min online test at the designated temperatures (see Figure S11).

In order to quantify the total amount of surface Ni-Co active sites available on R-PBMCN10 and R-PBMCN20 surfaces, we performed the CO pulse chemisorption analysis (see the results in Table S4). Indeed, R-PBMCN10 exhibited a higher metal surface area (4.93 m^2 g^{-1}) than R-PBMCN20 (2.36 m^2 g^{-1}) despite the fact that the amount of the exsolved bimetallic nanoparticles in R-PBMCN20 was much higher (cf. the XRD refinement results). This abnormal phenomenon was due to the partial blockage of the exsolved Ni-Co sites in R-PBMCN20 by the decomposed layer as shown in the XPS results. In the stability test, we first selected the conditions at which the conversions were well below the thermodynamic equilibrium by increasing the flow rates and decreasing the catalyst loadings (see Figure 5c).[44] R-PBMCN20 still showed better activity in comparison with R-PBMCN10. Little performance degradations for both R-PBMCN10 and R-PBMCN20 have been observed during 24 h on stream at 850 °C. We also calculated the values of turnover frequency (TOF), defined as the number of CH_4 molecules converted
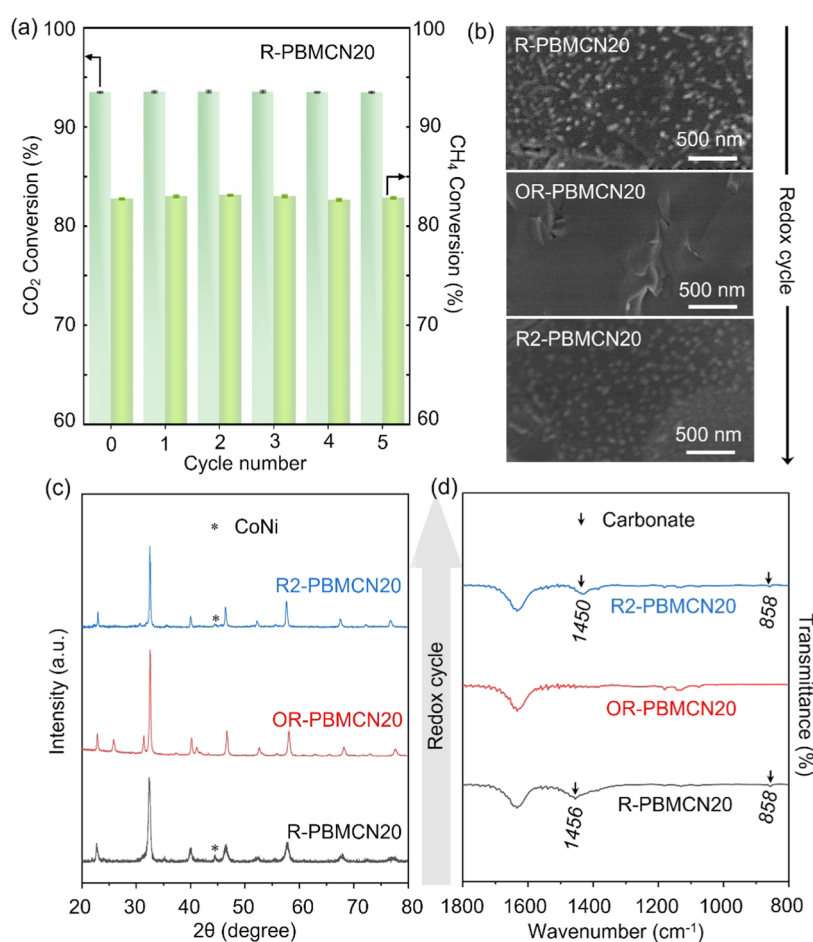
Figure 6. (a) CO_2 and CH_4 conversion of R-PBMCN20 in DRM after redox cycles; the feedstock is $CH_4/CO_2/N_2$ = 10:10:80 mL min^{-1}; catalyst loading is 70 mg; (b) SEM images of R-PBMCN20 during the redox cycle; (c) XRD patterns and (d) FTIR spectra of R-PBMCN20, OR-PBMCN20, and R2-PBMCN20.

per second per Ni-Co alloy active site (see Figure 5d). Although R-PBMCN20 showed a higher TOF, we maintained that the intrinsic activity of the Ni-Co alloy active site in both catalysts should be essentially identical in theory. The nominal difference might be originated from the catalyst surface reconstruction that changed the metal surface area *in situ*.

We also compared the longevity performance between R-PBMCN20 and the industrial-supported Ni catalyst. Albeit the conventional Ni/Al$_2$O$_3$ catalyst (20 wt % Ni on Al$_2$O$_3$, see Figure 5e) showing better initial activity compared with that of R-PBMCN20 at 850 °C, the latter, however, was much more stable during the 50 h longevity test compared with the Ni/Al$_2$O$_3$ catalyst. The rapid degradation of Ni/Al$_2$O$_3$ was ascribed to the coking of Ni nanoparticles. The formed coke caused the structural disintegration of the supported metal catalyst and gradually blocked the flow reactor. Note that this comparison does not reflect the fact that the exsolved nanoparticles were intrinsically more stable or active than the conventionally prepared Ni nanoparticles, as other parameters, such as the nature of the support, the Ni content, and the particle size, will also influence the coking resistance.

In addition to the improved activity and stability, a key advantage of the catalysts prepared *via* exsolution is their capability of easy regeneration. We thus carried out five redox cycles for R-PBMCN20. The catalytic performance in DRM after each cycle is presented in Figure 6a. Interestingly, ~94%

conversion of CO_2 and ~83% conversion of CH_4 were maintained without apparent degradation. We also characterized the chemico-physical properties of the catalyst during the redox cycle. From the SEM images in Figure 6b, we noticed that after the calcination (sample denoted as OR-PBMCN20), a clean fractural surface was retrieved. After the sequential reduction (sample denoted as R2-PBMCN20), well-dispersed nanostructures reappeared. TEM analysis confirmed that such nanostructures were still pure Ni-Co bimetallic NPs. This morphological evolution implied that the metallic nanoparticle exsolution-dissolution of the surface-decomposed perovskite might remain highly reversible.

This deduction was further confirmed by additional characterizations. The XRD patterns in Figure 6c show that, after the calcination at 950 °C, both the exsolved Ni-Co NPs and BaO, together with other nanocrystals, "re-dissolved" into the PBM perovskite host, forming a single-phase material. The carbonate peak was negligible, implying the complete decomposition of BaCO$_3$. Note that this decomposition temperature was greatly lower than that of the bulk BaCO$_3$, plausibly due to the quantum effect of the small nanostructure.[38,45] Our FTIR analysis also confirmed the complete decomposition of the carbonate (see Figure 6d). Sequential reduction of the OR-PBMCN20 (the resulting sample was denoted as R2-PBMCN20) also induced the formation of exsolved Ni-Co NPs and the Ba-rich phase.
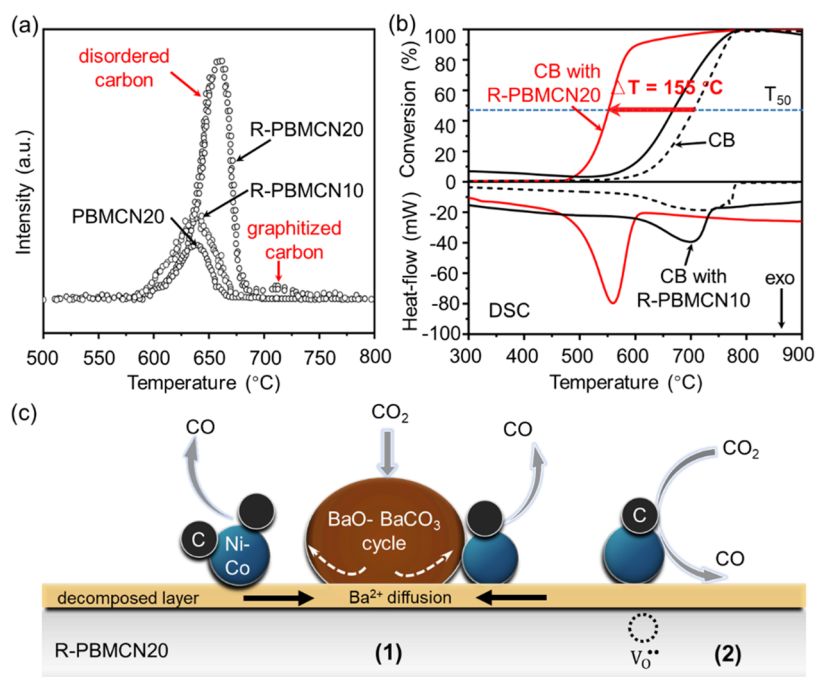
Figure 7. (a) O_2-TPO of the spent catalysts, (b) TGA−DSC curves of carbon black (CB) oxidation (dotted line) with R-PBMCN10 (black solid line) and with R-PBMCN20 (red solid line), and (c) schematic routes of $BaCO_3$ formation and coke removal in R-PBMCN20, $V_O^{\bullet\bullet}$/oxygen vacancies.

2.4. Activity Study of Surface-Decomposed R-PBMCN20 vs Surface-Intact R-PBMCN10. As we have shown before that the surface decomposition layer has partially blocked Ni-Co NPs in R-PBMCN20, then why R-PBMCN20 performed better than the surface-intact R-PBMCN10 in DRM? To gain more insights, the spent catalysts after the stability test in DRM reaction were first analyzed by the temperature-programmed oxidation (O_2-TPO, see Figure 7a). PBMCN20 and R-PBMCN10 exhibited a substantially weaker peak than that of R-PBMCN20, reflecting that R-PBMCN20 might contain more active sites for carbon deposition. This speculation was further verified by XPS analysis of the oxidized spent catalyst. R-PBMCN20 indeed demonstrated higher surface Ni content (0.7 atom %) than that of R-PBMCN10 (0.3 atom %). Note that in the TPO profile, R-PBMCN20 demonstrated two oxidation peaks. The peak at ~600 °C was much stronger, corresponding to the amorphous carbon, which can be readily removed by CO_2. The other peak that started at ~700 °C was negligible, suggesting essentially no formation of graphitic carbon.[46] This result was aligned with the good carbon resistance of R-PBMCN20.

We then evaluated the capability of the catalysts for removing deposited carbon using TGA−DSC. Carbon black (CB) was added to the fresh catalysts (10 wt %). Since it was obtained from the thermal cracking of ethylene tar, it was an ideal carbon source to simulate the coke. The homogenized mixture was then heated up in the stream of air. Figure 7b shows the typical CB conversion and DSC curves. Pure carbon black was also assessed as the control experiment. The temperature at which 50% CB was converted (denoted as T_{50}) was used as the benchmark to demonstrate the activity of the catalyst. The addition of the R-PBMCN20 catalyst effectively lowered the coke ignition temperature, with the T_{50} value decreasing by about 155 °C. The huge exothermic reaction occurred at 560 °C was ascribed to the fast coke oxidation.

Above 560 °C, the conversion rate increases slowly, which can be ascribed to the oxidation of either graphitic carbon or the catalyst itself. However, the catalytic effect of R-PBMCN10 was not as prominent as that of R-PBMCN20.

Based on the above-mentioned results, the hypothetical mechanism for the increased activity and coking resistance of R-PBMCN20 was proposed. A graphical illustration is depicted in Figure 7c. In DRM, the presence of CO_2 and steam at high temperature enabled the fast diffusion of Ba^{2+} and formation of large $BaCO_3$ domains in this surface-decomposed catalyst; the Ni-Co sites previously blocked by the decomposition layer were then recovered for catalysis (*cf.* XPS results). Because R-PBMCN20 contained more Ni-Co sites, higher activity was observed in DRM. The good coking resistance might be related to the presence of surface barium species: the $BaCO_3$ domains decomposed at higher temperature to form BaO, which behaved as the catalytic promoter, offering basicity for much stronger CO_2 adsorption capacity.[47] The electron transfer from the promoter also increases the electron cloud density of the adjacent metallic NP.[48] Both effects will concurrently accelerate the CO_2 activation rate on the catalyst surface, prohibiting the formation of graphitic coke. Note that the isolated Ni-Co bimetallic site in R-PBMCN20 (position 2) was also coke resistant. The $PrBaMn_2O_{5+\delta}$ support was oxygen-deficient, with proven capability of accelerating the adsorption and activation of CO_2.[49,50] The deposited carbon on this site, if any, can also be oxidized by the lattice oxygen from the support *via* the well-known Mars−Van Krevelen mechanism.[51] In conclusion, we proposed that the DRM reaction condition facilitated the diffusion of Ba^{2+}, recovering the previously blocked active sites for catalysis. As the Ni-Co sites in R-PBMCN20 are more abundant than those in R-PBMCN10 (see the XRD refinement and XPS results), it is thus natural to observe better activity in R-PBMCN20.

3. CONCLUSIONS

The *in situ* exsolution of Ni-Co NPs from $Pr_{0.45}Ba_{0.45}Mn_{1-x}(Co_{1/3} Ni_{2/3})_xO_{3\pm\delta}$ induced the surface decomposition when x reached 0.2, forming a thin layer comprising various nanocrystalline oxides that partially blocked the active sites of exsolved Ni-Co particles. A quantitative study revealed that ∼7.2 wt % of perovskite has decomposed. A hydration and carbonation reaction facilitated the migration of nanocrystalline BaO species and the formation of large and highly crystalized $BaCO_3$, enabling the recovery of blocked Ni-Co active sites. The surface-decomposed catalyst remained highly active in the dry methane reforming reaction with better stability. Importantly, the metallic nanoparticle regeneration feature was not hampered in this surface-decomposed perovskite as the complete exsolution-dissolution recyclability remained. This work offered a simple strategy of quantitatively determining the fraction of decomposed Ba-containing perovskite oxide on the surface, offering new insights into the behaviors of exsolved catalysts with surface decomposition.

4. EXPERIMENTAL SECTION

4.1. Material Preparation. $Pr(NO_3)_3 \cdot 6H_2O$, $Ba(NO_3)_2$, $Ni(NO_3)_2 \cdot 6H_2O$, ethylene glycol $(C_2H_4O_2H_2)$, and absolute alcohol were purchased from Sinopharm Chemical Reagent Co., Ltd. $Co(NO_3)_2 \cdot 6H_2O$, $Mn(NO_3)_2$ solution (50 wt % in H_2O), and citric acid monohydrate $(C_6H_8O_7 \cdot H_2O)$ were purchased from Aladdin. γ-Al_2O_3 catalyst support was obtained from Sigma-Aldrich. All chemicals were of analytical grade and used without further purification.

A-site-deficient $Pr_{0.45}Ba_{0.45}MnO_{3\pm\delta}$ doped with 20 mol % Co-Ni (Co/Ni =1:2) at the B-site was prepared by a modified sol−gel method. The stoichiometric amounts of Pr, Ba, Mn, Ni, and Co nitrates were dissolved in distilled water under stirring for about 30 min. Ethylene glycol and citric acid were then added to serve as the complexing agents. The molar ratio of total metal ions to ethylene glycol to citric acid was set at 1:1.5:3. The solution was magnetically stirred at 80 °C in a water bath until the gel formed. Then, the gel was dried at 60 °C in an oven and then heated at 350 °C for 2 h to form a solid precursor. Subsequently, the obtained black powder was calcined at 950 °C for 5 hours in the air to form PBMCN. The reduction of the oxide was performed by annealing PBMCN in 5% H_2-95% Ar at 800 °C for 4 h. This prepared material was denoted as R-PBMCN. The carbonation was carried out by aging R-PBMCN in humidified air (RH = 98%) for 20 days; the resulting material was denoted as AR-PBMCN.

To prepare the commercial 20 wt % Ni/Al_2O_3, a wet-impregnation approach was applied. Before use, γ-Al_2O_3 powder was initially grinded and dried at 120 °C overnight. A certain amount of $Ni(NO_3)_2 \cdot 6H_2O$ was dissolved in 20 mL of deionized H_2O and stirred vigorously; then, 10 g of pretreated γ-Al_2O_3 was added to the solution. The suspension was stirred at room temperature for 4 h in a 100 mL round-bottom flask and then was heated in an oil bath at 60 °C to evaporate the water. The obtained solid was scratched down and grinded in a mortar into fine powder. The powder was further dried in an oven at 120 °C for 6 h. The catalyst was calcined under airflow at 500 °C for 5 h and reduced at 650 °C in 5% H_2-95% Ar for 1 h.

4.2. Material Characterizations. X-ray diffraction analysis (XRD, Rigaku SmartLab) was carried out using a Cu Kα radiation source (λ = 1.5418 Å) operating at a tube voltage of 40 kV and a current of 40 mA. Diffraction patterns were collected by step scanning with the scan rate of 4° min^{-1} and in the 2θ range of 20−80°. Rietveld refinement was performed by using a fullprof program. Oxygen vacancies were not introduced into the refinement calculation because of the small scattering cross section of the oxygen. In the Fourier-transform infrared spectroscopy (FTIR) analysis, 1 mg of sample powder was mixed with 200 mg of KBr powder and pressed into a thin pellet using a stainless-steel die. FTIR signals were collected from 4000 to 400 cm^{-1} using a Bruker INVENIO-R spectrometer. The morphologies of the oxide powders were investigated by field-emission scanning electron microscopy (FE-SEM, Hitachi S-4800). Transmission electron microscopy (TEM, JEM-F200) was used to further investigate and analyze the microstructural morphology and composition. It was equipped with an HAADF detector coupled with an X-ray energy dispersive spectrometer (EDS) for elemental analysis. The surface chemistry was analyzed by a X-ray photoelectron spectroscopy (XPS, ESCALab 250Xi Thermo Scientific) with Al Kα ($h\nu$ = 1486.6 eV) radiation; the base pressure of the analytical chamber during the measurements was lower than 3.0×10^{-9} mbar. The spectra of survey scan were recorded with the pass energy of 150.0 eV; the energy step size was 1.000 eV. High-resolution spectra were recorded with the pass energy of 60.0 eV, and the energy step size was 0.100 eV. All of the binding energies were calibrated to the adventitious C 1s peak at 284.8 eV. The deconvolution was carried out using the Thermo Avantage software package. A smart-type background subtraction and a Gaussian-Lorentzian peak shape were applied.

The thermogravimetric and differential scanning calorimetric analysis (TGA−DSC, NETZSCH STA 449F5) was performed in an air atmosphere with a flow rate of 100 mL min^{-1}. The temperature range was 25−900 °C, and the heating rate was 10 °C min^{-1}. Carbon black, as a simulated coke substance, was mixed with the catalyst in an agate mortar (catalyst to carbon 9:1) to obtain a homogeneous mixture. TPO was performed using the Thermo Scientific TPDRO 1100 instrument with a thermal conductivity detector (TCD). 10 mg of the catalyst was loaded to the quartz tube reactor, and all of the measurements were carried out in a stream of O_2 (40 mL min^{-1}) with a heating rate of 10 °C min^{-1}.

The CO pulse chemisorption was carried out using an AutoChem II 2920 apparatus (Micromeritics). The samples were reduced under a 5% H_2/He gas (30 mL/min) at 450 °C for 1 h, then purged with helium (30 mL/min) for 30 min before the temperature was decreased to 50 °C for CO pulse adsorption. 0.5 mL of CO pulse was repeatedly injected into the sampling chamber until no further CO uptakes were detected between consecutive injections. The number of active sites available in the catalyst was measured based on the cumulative quantity of adsorbed CO, which was correlated to the metal surface area (S_{msa}) of the sample. Metal dispersion (D) of the sample, defined as the ratio of the number of active sites available to the total amount of active metals in the catalyst, was obtained based on the results of S_{msa}.

4.3. Catalytic Reaction. DRM was performed in a continuous-flow fixed-bed reactor at ambient pressure. The internal diameter of the quartz tube was 4 mm, which was mounted in an insulated electric furnace equipped with a programmable temperature controller (Eurotherm GmbH). Approximately 70 mg of sample powder was placed in the middle of the reactor. For the DRM test, a gas mixture of CO_2, CH_4, and N_2 was introduced into the reactor with a ratio of 10:10:80. The gas flow was controlled by a mass flow controller. The gas hourly space velocity (GHSV) was 8.57×10^3 mL h^{-1} g^{-1}, which is higher than or comparable to those in the literature. The reaction products were analyzed online using a gas chromatograph (Compact GC 4.0) equipped with a thermal conductivity detector (TCD). The DRM reaction is shown below: the CH_4 and CO_2 conversion were as shown in the following equations

$$CH_4 + CO_2 \rightarrow 2CO + 2H_2 (\Delta H^0_{298\,K} = 247\ kJ/mol) \quad (5)$$

$$CH_4\ conversion = \frac{CH_{4\,in} - CH_{4\,out}}{CH_{4\,in}} \times 100\% \quad (6)$$

$$CO_2\ conversion = \frac{CO_{2\,in} - CO_{2\,out}}{CO_{2\,in}} \times 100\% \quad (7)$$

whereas $CH_{4\,in}$ and $CH_{4\,out}$ are the mol % of inlet and outlet methane; $CO_{2\,in}$ and $CO_{2\,out}$ are the mol % of the inlet and outlet carbon dioxide.

The turnover frequency (TOF) of the catalyst in DRM was defined as the number of CH_4 molecules converted per second per Ni-Co alloy active site. The Ni-Co alloy active sites were determined based on the CO pulse chemisorption results. To enable a more accurate calculation of TOF, we increased the space velocity of the reactor (reaction conditions: GHSV = 3.00×10^4 mL h^{-1} g^{-1}, with 50 mg of catalyst powder and a gas flow rate ratio of 25:25:50 for CH_4, CO_2 and N_2), so the conversions of both CH_4 and CO_2 were maintained well below the thermodynamic equilibrium values at 850 °C.[44] Equa-Equation 8 below was used for the calculation

$$TOF = F \times \chi / (W \times R \times D) \tag{8}$$

where F (mole/s) is the flow rate of CH_4, the reactant; χ (%) is the conversion; W (g) is the total mass of the loaded catalyst; R (mole/g) is the ratio of metal loading in the catalyst; and D (%) is the metal dispersion.

ASSOCIATED CONTENT

Supporting Information

The Supporting Information is available free of charge at https://pubs.acs.org/doi/10.1021/acs.chemmater.2c02488.

Additional data including XRD, XPS, TEM images, FTIR spectra and catalytic test results (PDF)

AUTHOR INFORMATION

Corresponding Author

Ning Yan − *School of Physics and Technology, Wuhan University, Wuhan 430072, China; Van't Hoff Institute for Molecular Sciences (HIMS), University of Amsterdam, Amsterdam 1098 XH, The Netherlands; Suzhou Institute of Wuhan University, Suzhou 215123, China;* orcid.org/0000-0001-6677-7507; Email: ning.yan@whu.edu.cn

Authors

Xiaojuan Cao − *School of Physics and Technology, Wuhan University, Wuhan 430072, China*

Le Ke − *School of Physics and Technology, Wuhan University, Wuhan 430072, China*

Kai Zhao − *School of Physics and Technology, Wuhan University, Wuhan 430072, China*

Xiaoyu Yan − *School of Physics and Technology, Wuhan University, Wuhan 430072, China*

Xiaoyu Wu − *School of Physics and Technology, Wuhan University, Wuhan 430072, China*

Complete contact information is available at:
https://pubs.acs.org/10.1021/acs.chemmater.2c02488

Notes

The authors declare no competing financial interest.

ACKNOWLEDGMENTS

REFERENCES

(1) Kattel, S.; Liu, P.; Chen, J. G. Tuning Selectivity of CO_2 Hydrogenation Reactions at the Metal/Oxide Interface. *J. Am. Chem. Soc.* **2017**, *139*, 9739−9754.

(2) Jiang, Z.; Sun, Z.; Yang, Y.; Chen, S.; Shangguan, W.; Wu, X. The role of metal oxide interactions: revisiting Pt growth on the TiO_2 surface in the process of impregnation method. *Nanoscale* **2017**, *9*, 14272−14279.

(3) Mateo, D.; Morlanes, N.; Maity, P.; Shterk, G.; Mohammed, O. F.; Gascon, J. Efficient Visible-Light Driven Photothermal Conversion of CO_2 to Methane by Nickel Nanoparticles Supported on Barium Titanate. *Adv. Funct. Mater.* **2021**, *31*, No. 2008244.

(4) Hunston, C.; Baudouin, D.; Tarik, M.; Kröcher, O.; Vogel, F. Investigating active phase loss from supported ruthenium catalysts during supercritical water gasification. *Catal. Sci. Technol.* **2021**, *11*, 7431−7444.

(5) Yeh, T.; Linic, S.; Savage, P. E. Deactivation of Pt Catalysts during Hydrothermal Decarboxylation of Butyric Acid. *ACS Sustainable Chem. Eng.* **2014**, *2*, 2399−2406.

(6) Ide, M. S.; Falcone, D. D.; Davis, R. J. On the deactivation of supported platinum catalysts for selective oxidation of alcohols. *J. Catal.* **2014**, *311*, 295−305.

(7) Liu, S.; Liu, Q.; Luo, J.-L. Highly Stable and Efficient Catalyst with In Situ Exsolved Fe-Ni Alloy Nanospheres Socketed on an Oxygen Deficient Perovskite for Direct CO2 Electrolysis. *ACS Catal.* **2016**, *6*, 6219−6228.

(8) Neagu, D.; Oh, T.-S.; Miller, D. N.; Ménard, H.; Bukhari, S. M.; Gamble, S. R.; Gorte, R. J.; Vohs, J. M.; Irvine, J. T. S. Nano-socketed nickel particles with enhanced coking resistance grown in situ by redox exsolution. *Nat. Commun.* **2015**, *6*, No. 8120.

(9) Wang, J.; Zhou, J.; Yang, J.; Neagu, D.; Fu, L.; Lian, Z.; Shin, T.-H.; Wu, K. Tailoring the Surface of Perovskite through In Situ Growth of Ru/RuO_2 Nanoparticles as Robust Symmetrical Electrodes for Reversible Solid Oxide Cells. *Adv. Mater. Interfaces* **2020**, *7*, No. 2070132.

(10) Nishihata, Y.; Mizuki, J.; Akao, T.; Tanaka, H.; Uenishi, M.; Kimura, M.; Okamoto, T.; Hamada, N. Self-regeneration of a Pd-perovskite catalyst for automotive emissions control. *Nature* **2002**, *418*, 164−167.

(11) Bekheet, M. F.; Delir Kheyrollahi Nezhad, P.; Bonmassar, N.; Schlicker, L.; Gili, A.; Praetz, S.; Gurlo, A.; Doran, A.; Gao, Y.; Heggen, M.; Niaei, A.; Farzi, A.; Schwarz, S.; Bernardi, J.; Klötzer, B.; Penner, S. Steering the Methane Dry Reforming Reactivity of Ni/La_2O_3 Catalysts by Controlled In Situ Decomposition of Doped La_2NiO_4 Precursor Structures. *ACS Catal.* **2021**, *11*, 43−59.

(12) Arandiyan, H.; Wang, Y.; Scott, J.; Mesgari, S.; Dai, H.; Amal, R. In Situ Exsolution of Bimetallic Rh−Ni Nanoalloys: a Highly Efficient Catalyst for CO_2 Methanation. *ACS Appl. Mater. Interfaces* **2018**, *10*, 16352−16357.

(13) Naeem, M. A.; Abdala, P. M.; Armutlulu, A.; Kim, S. M.; Fedorov, A.; Müller, C. R. Exsolution of Metallic Ru Nanoparticles from Defective, Fluorite-Type Solid Solutions $Sm_2Ru_xCe_{2−x}O_7$ To Impart Stability on Dry Reforming Catalysts. *ACS Catal.* **2020**, *10*, 1923−1937.

(14) Kim, M.; Park, J.; Ju, H.; Kim, J. Y.; Cho, H.-S.; Kim, C.-H.; Kim, B.-H.; Lee, S. W. Understanding synergistic metal−oxide interactions of in situ exsolved metal nanoparticles on a pyrochlore oxide support for enhanced water splitting. *Energy Environ. Sci.* **2021**, *14*, 3053−3063.

(15) Tang, L.; Chen, Z.; Zuo, F.; Hua, B.; Zhou, H.; Li, M.; Li, J.; Sun, Y. Enhancing perovskite electrocatalysis through synergistic functionalization of B-site cation for efficient water splitting. *Chem. Eng. J.* **2020**, *401*, No. 126082.

(16) Huang, R.; Lim, C.; Jang, M. G.; Hwang, J. Y.; Han, J. W. Exsolved metal-boosted active perovskite oxide catalyst for stable water gas shift reaction. *J. Catal.* **2021**, *400*, 148−159.

(17) Su, C.; Wang, W.; Shao, Z. Cation-Deficient Perovskites for Clean Energy Conversion. *Acc. Mater. Res.* **2021**, *2*, 477−488.

(18) Neagu, D.; Tsekouras, G.; Miller, D. N.; Ménard, H.; Irvine, J. T. S. In situ growth of nanoparticles through control of non-stoichiometry. *Nat. Chem.* **2013**, *5*, 916−923.

(19) Cai, Z.; Kubicek, M.; Fleig, J.; Yildiz, B. Chemical Heterogeneities on $La_{0.6}Sr_{0.4}CoO_{3−\delta}$ Thin Films—Correlations to Cathode Surface Activity and Stability. *Chem. Mater.* **2012**, *24*, 1116−1127.

(20) Jung, W.; Tuller, H. L. Investigation of surface Sr segregation in model thin film solid oxide fuel cell perovskite electrodes. *Energy Environ. Sci.* **2012**, *5*, 5370–5378.

(21) Téllez, H.; Druce, J.; Kilner, J. A.; Ishihara, T. Relating surface chemistry and oxygen surface exchange in LnBaCo₂O₅₊δ air electrodes. *Faraday Discuss.* **2015**, *182*, 145–157.

(22) Hua, B.; Sun, Y.-F.; Li, M.; Yan, N.; Chen, J.; Zhang, Y.-Q.; Zeng, Y.; Shalchi Amirkhiz, B.; Luo, J.-L. Stabilizing Double Perovskite for Effective Bifunctional Oxygen Electrocatalysis in Alkaline Conditions. *Chem. Mater.* **2017**, *29*, 6228–6237.

(23) Sun, Y.-F.; Li, J.-H.; Zhang, Y.-Q.; Hua, B.; Luo, J.-L. Bifunctional Catalyst of Core−Shell Nanoparticles Socketed on Oxygen-Deficient Layered Perovskite for Soot Combustion: In Situ Observation of Synergistic Dual Active Sites. *ACS Catal.* **2016**, *6*, 2710–2714.

(24) Hua, B.; Yan, N.; Li, M.; Sun, Y. F.; Zhang, Y. Q.; Li, J.; Etsell, T.; Sarkar, P.; Luo, J. L. Anode-Engineered Protonic Ceramic Fuel Cell with Excellent Performance and Fuel Compatibility. *Adv. Mater.* **2016**, *28*, 8922–8926.

(25) Pang, S.; Yang, G.; Jiang, X.; Shen, X.; Rao, D.; Chen, C. Insight into tuning the surface and bulk microstructure of perovskite catalyst through control of cation non-stoichiometry. *J. Catal.* **2020**, *381*, 408–414.

(26) Zhang, Z.-X.; Xie, X.-B.; Xu, Q.; Huang, D.-P.; Chen, M.; Zhao, K.; Chen, D.-C.; Zhang, F. Alleviated surface calcium segregation and improved electrocatalytic properties of La₀.₃Ca₀.₇Fe₀.₇Cr₀.₃O₃₋δ cathode: A demonstration of A-site deficiency effect. *J. Alloys Compd.* **2022**, *924*, No. 166615.

(27) Chen, Y.; Fong, D. D.; Herbert, F. W.; Rault, J.; Rueff, J.-P.; Tsvetkov, N.; Yildiz, B. Modified Oxygen Defect Chemistry at Transition Metal Oxide Heterostructures Probed by Hard X-ray Photoelectron Spectroscopy and X-ray Diffraction. *Chem. Mater.* **2018**, *30*, 3359–3371.

(28) Zhu, Y.; Zhang, L.; Zhao, B.; Chen, H.; Liu, X.; Zhao, R.; Wang, X.; Liu, J.; Chen, Y.; Liu, M. Improving the Activity for Oxygen Evolution Reaction by Tailoring Oxygen Defects in Double Perovskite Oxides. *Adv. Funct. Mater.* **2019**, *29*, No. 1901783.

(29) Park, S.; Kim, Y.; Noh, Y.; Kim, T.; Han, H.; Yoon, W.; Choi, J.; Yi, S.-H.; Lee, W.-J.; Kim, W. B. A sulfur-tolerant cathode catalyst fabricated with in situ exsolved CoNi alloy nanoparticles anchored on a Ruddlesden−Popper support for CO₂ electrolysis. *J. Mater. Chem. A* **2020**, *8*, 138–148.

(30) Fagerlund, J.; Highfield, J.; Zevenhoven, R. Kinetics studies on wet and dry gas−solid carbonation of MgO and Mg(OH)₂ for CO₂ sequestration. *RSC Adv.* **2012**, *2*, 10380–10393.

(31) Wang, C.; Jia, L.; Tan, Y.; Anthony, E. J. The Effect of Water on the Sulphation of Limestone. *Fuel* **2010**, *89*, 2628–2632.

(32) Guo, H.; Yan, S.; Zhao, Y.; Ma, X.; Wang, S. Influence of water vapor on cyclic CO₂ capture performance in both carbonation and decarbonation stages for Ca-Al mixed oxide. *Chem. Eng. J.* **2019**, *359*, 542–551.

(33) Zarghami, S.; Hassanzadeh, A.; Arastoopour, H.; Abbasian, J. Effect of Steam on the Reactivity of MgO-Based Sorbents in Precombustion CO₂ Capture Processes. *Ind. Eng. Chem. Res.* **2015**, *54*, 8860–8866.

(34) Wang, N.; Feng, Y.; Guo, X.; van Duin, A. C. T. Insights into the Role of H₂O in the Carbonation of CaO Nanoparticle with CO₂. *J. Phys. Chem. C* **2018**, *122*, 21401–21410.

(35) Rodriguez-Blanco, J. D.; Shaw, S.; Benning, L. G. The kinetics and mechanisms of amorphous calcium carbonate (ACC) crystallization to calcite, viavaterite. *Nanoscale* **2011**, *3*, 265–271.

(36) Ren, F.; Ding, Y.; Leng, Y. Infrared spectroscopic characterization of carbonated apatite: A combined experimental and computational study. *J. Biomed. Mater. Res., Part A* **2014**, *102*, 496–505.

(37) Boston, R.; Schnepp, Z.; Nemoto, Y.; Sakka, Y.; Hall, S. R. In Situ TEM Observation of a Microcrucible Mechanism of Nanowire Growth. *Science* **2014**, *344*, 623–626.

(38) Yan, N.; Gao, T.; Wang, W.; Luo, J. L. Understanding the Aging Degradation of Doped Barium Cerate Proton Conductor in Ambient Air at Room Temperature. *ECS Trans.* **2015**, *68*, 457–466.

(39) Yu, Y.; Ludwig, K. F.; Woicik, J. C.; Gopalan, S.; Pal, U. B.; Kaspar, T. C.; Basu, S. N. Effect of Sr Content and Strain on Sr Surface Segregation of La₁₋ₓSrₓCo₀.₂Fe₀.₈O₃₋δ as Cathode Material for Solid Oxide Fuel Cells. *ACS Appl. Mater. Interfaces* **2016**, *8*, 26704–26711.

(40) Chen, Y.; Téllez, H.; Burriel, M.; Yang, F.; Tsvetkov, N.; Cai, Z.; McComb, D. W.; Kilner, J. A.; Yildiz, B. Segregated Chemistry and Structure on (001) and (100) Surfaces of (La₁₋ₓSrₓ)₂CoO₄ Override the Crystal Anisotropy in Oxygen Exchange Kinetics. *Chem. Mater.* **2015**, *27*, 5436–5450.

(41) Druce, J.; Téllez, H.; Burriel, M.; Sharp, M. D.; Fawcett, L. J.; Cook, S. N.; McPhail, D. S.; Ishihara, T.; Brongersma, H. H.; Kilner, J. A. Surface termination and subsurface restructuring of perovskite-based solid oxide electrode materials. *Energy Environ. Sci.* **2014**, *7*, 3593–3599.

(42) Téllez, H.; Druce, J.; Ju, Y.-W.; Kilner, J.; Ishihara, T. Surface chemistry evolution in LnBaCo₂O₅₊δ double perovskites for oxygen electrodes. *Int. J. Hydrogen Energy* **2014**, *39*, 20856–20863.

(43) Lu, M.; Zhang, X.; Deng, J.; Kuboon, S.; Faungnawakij, K.; Xiao, S.; Zhang, D. Coking-resistant dry reforming of methane over BN−nanoceria interface-confined Ni catalysts. *Catal. Sci. Technol.* **2020**, *10*, 4237–4244.

(44) Jafarbegloo, M.; Tarlani, A.; Mesbah, A. W.; Sahebdelfar, S. Thermodynamic analysis of carbon dioxide reforming of methane and its practical relevance. *Int. J. Hydrogen Energy* **2015**, *40*, 2445–2451.

(45) Arvanitidis, I.; Siche, D.; Seetharaman, S. A study of the thermal decomposition of BaCO₃. *Metall. Mater. Trans. B* **1996**, *27*, 409–416.

(46) González, D.; Altin, O.; Eser, S.; Garcia, A. B. Temperature-programmed oxidation studies of carbon materials prepared from anthracites by high temperature treatment. *Mater. Chem. Phys.* **2007**, *101*, 137–141.

(47) Alipour, Z.; Rezaei, M.; Meshkani, F. Effect of alkaline earth promoters (MgO, CaO, and BaO) on the activity and coke formation of Ni catalysts supported on nanocrystalline Al₂O₃ in dry reforming of methane. *J. Ind. Eng. Chem.* **2014**, *20*, 2858–2863.

(48) Zhou, J.; Ma, H.; Jin, F.; Zhang, H.; Ying, W. Mn and Mg dual promoters modified Ni/α-Al₂O₃ catalysts for high temperature syngas methanation. *Fuel Process. Technol.* **2018**, *172*, 225–232.

(49) Zhang, J.; Yin, R.; Shao, Q.; Zhu, T.; Huang, X. Oxygen Vacancies in Amorphous InOx Nanoribbons Enhance CO₂ Adsorption and Activation for CO₂ Electroreduction. *Angew. Chem., Int. Ed.* **2019**, *58*, 5609–5613.

(50) Wang, Y.; Chen, Z.; Han, P.; Du, Y.; Gu, Z.; Xu, X.; Zheng, G. Single-Atomic Cu with Multiple Oxygen Vacancies on Ceria for Electrocatalytic CO₂ Reduction to CH₄. *ACS Catal.* **2018**, *8*, 7113–7119.

(51) Wang, C.; Gu, X.-K.; Yan, H.; Lin, Y.; Li, J.; Liu, D.; Li, W.-X.; Lu, J. Water-Mediated Mars−Van Krevelen Mechanism for CO Oxidation on Ceria-Supported Single-Atom Pt₁ Catalyst. *ACS Catal.* **2017**, *7*, 887–891.